Using cohesive zone models with digital image correlation to obtain a mixed mode I/II fracture envelope of a tough epoxy

Christopher M. Jackson[a], Jeffrey A. McGuire[b], Martin Losada[c], Ian Maskery[d], Ian Ashcroft[d], Raffaella De Vita[b], David A. Dillard[b]

[a] *Civil and Environmental Engineering, Virginia Tech, Blacksburg, 24061, VA, USA*
[b] *Biomedical Engineering and Mechanics, Virginia Tech, Blacksburg, 24061, VA, USA*
[c] *Coatings Innovation Center, PPG Industries, Inc., Allison Park, 15101, PA, USA*
[d] *Mechanical, Materials and Manufacturing Engineering, Faculty of Engineering, Univeristy of Nottingham, Nottingham, NG8 1BB, UK*

Abstract

This work describes a method in which the digital image correlation (DIC) method and finite element analysis (FEA) were used to create a quasi-static mixed-mode fracture envelope for bonded joints consisting of 2024-T3 Al adherends and a tough structural epoxy adhesive. Symmetric and asymmetric versions of double cantilever beam, single-leg bend, and end-notched flexure tests are used to populate the mixed-mode fracture envelope with results at several mode mixities. Experiments are conducted in a universal testing machine while recording images for subsequent DIC analysis. Finite element analysis is used to implement cohesive zone models (CZMs) of the adhesive fracture and to account for plastic deformation of adherends. Mode I and mode II traction separation laws (TSLs) are determined from a property identification method with a Benzeggagh-Kenane mixed-mode coupling law used to model mixed-mode behavior. FEA results are shown to provide a good agreement to both the crosshead displacement and DIC data. The methods in this paper serve as a potential framework for future calibration of mixed-mode fracture envelopes for joints bonded with very tough adhesives that complicate assessment with traditional data analysis methods.

Keywords: Fracture mechanics, Mixed mode fracture, Digital image correlation, Cohesive zone modeling
PACS: 0000, 1111
2000 MSC: 0000, 1111

Abbreviations

$BoEF$ Beam on elastic foundation

$CBBM$ Compliance-Based Beam Method

CBT Corrected Beam Theory

CLS Cracked lap shear

$CMOD$ Crack mouth opening displacement

CZM Cohesive Zone Model

DCB Double cantilever beam

DIC Digital image correlation

ECM Experimental Compliance Method

ENF End notched flexure

FEA Finite element analysis

$LEFM$ Linear Elastic Fracture Mechanics

SBT Simple Beam Theory

SLB Single leg bend

SLJ Single lap joint

TSL Traction Separation Law

Nomenclature

δ Crosshead displacement

$\epsilon_{xx}, \epsilon_{yy}, \epsilon_{xy}$ In-plane surface strains

ν Poisson's ratio

θ Relative rotation between double cantilever beam arms at load points

a	Crack length
a_p	Precrack length
B	Adherend and adhesive layer width
E	Elastic modulus
G	Shear modulus
G_c	Fracture energy
$G_{I/IIc}$	Mixed Mode I/II fracture energy
G_{Ic}	Mode I fracture energy
G_{IIc}	Mode II fracture energy
J	Rice's J-integral
L	Specimen length metric (as defined in Figure 1)
P	Load
P_w	Load per unit width
t_n, t_s	Tractions (normal and shear)

1. Introduction

A common concern with adhesively bonded joints is their resistance to fracture, including within the mixed-mode region between modes I and II that is typically experienced in bonded structures. In monolithic, isotropic materials, cracks generally grow in mode I fracture, and conventional wisdom is that mode I is usually the most critical loading mode for adhesively bonded systems as well [1, 2, 3, 4]. Because the crack is often confined to grow within an adhesive layer, however, cracks growing under general loading conditions may globally appear to propagate within the bondline in combinations of fracture modes. Although common for mode I fracture energies to be smaller, exceptions have been reported for several systems, such as when small mode II contributions effectively steer cracks out of dissipative adhesive layers [5, 6, 7]. Proper analysis of actual joint geometries subjected to complex loading often emphasize the importance of characterizing a mixed-mode fracture envelope that is then used to design bonded joints that can safely carry expected loads. And, if the mixed mode fracture energy is larger than the mode I fracture energy (i.e. $G_{I/IIc} > G_{Ic}$), these larger values may enable the construction of lighter structures for mixed mode loading scenarios.

The double cantilever beam (DCB) specimen [8, 9] is perhaps the most commonly used test to acquire mode I fracture energies in bonded and laminated materials, with the end-notched flexure (ENF) [10] or end-loaded split (ELS) [11] tests often being utilized to obtain mode II fracture energies. For regions between these two pure modes, some researchers have used the mixed-mode bend (MMB) test [12, 13]. Alternative techniques employed to acquire mixed-mode I/II fracture data are the single leg bend (SLB) test developed by Davidson and Sundararaman [14] and the cracked lap shear (CLS) configuration [15, 16, 4]. Asymmetric adherend thickness variations of any of these geometries can induce small variations of mode-mix, as discussed for example for DCB [17, 18, 19, 20] and SLB tests [21]. Special fixtures have been developed that allow fracture testing at various mode mixities [22, 23], as have dual-axis load frames to independently control mode mixity [24, 25, 26].

To acquire fracture energies from tests such as these, various closed-form, linear elastic fracture mechanics (LEFM) solutions and refinements have been developed by specimen proponents and practitioners. General approaches have been suggested for analyzing the mechanics of different joint configurations, including for partitioning mode mixity [27, 2]. Experimental implementation of such analyses for data reduction and fracture energy deter-

mination involve methods including the corrected beam theory (CBT) [28], the experimental compliance method (ECM) [29], and the compliance-based beam method (CBBM) [30, 31, 32]. These methods are easy to implement and program into either a spreadsheet [33] or code to facilitate calculation of fracture energies. These methods typically involve the collection of force and crosshead displacement values at discrete crack lengths, a, as fracture proceeds. While most of these methods also require crack length, it should be noted that the CBBM does not require that crack lengths be recorded, as it calculates an effective crack length based on specimen compliance. These data analysis methods have been widely used but are generally limited to cases where adherend deformations remain linear elastic.

An alternate method for acquiring fracture energy is Rice's J-integral [34] approach, which can be used for both linear and non-linear analysis, as recently discussed by Marzi [35]. Paris and Paris [36] derived a closed-form solution by applying Rice's J-integral to the DCB test configuration, demonstrating that J is equal to the applied load per unit width of bond, P_w, times the relative rotation angle between the two adherends at the point of load application, θ. This $P_w\theta$ method has rapidly gained attention, as practitioners have applied it to an increasingly broad range of adhesive systems [37, 38, 39, 40]. As LEFM solutions are a special form of the J-integral, both methods are treated as equivalent when conditions are largely linear-elastic. Recent mode I studies by Sun and Blackman have shown that for tough adhesives, assessing crack length estimates using DIC deflections can improve measurement accuracy of fracture energy, G_c, bringing CBT results into good agreement with the J-integral for several toughened epoxy adhesives [41]. For a ductile polyurethane adhesive, however, their G_{Ic} values still exceeded J_{Ic} by 15% [42]. This is likely because the large fracture process zone produced by such ductile adhesives deviates from the assumptions used in LEFM, as explained by [35].

The fracture energy of adhesives is important for design and resulting performance of bonded structures, and modern automotive, military, and other applications often benefit from increasing values of toughness to effectively access the potential energy dissipation capabilities of structures [43, 44]. Attempts to use existing test methods to evaluate the increasingly tougher adhesives being developed has met some limitations. Reported results in the literature are typically obtained with adherends that are sufficiently strong to nominally avoid plastic or other inelastic bending and the resulting complications. Most of the analytical models for interpreting adhesive fracture

specimen results are based on the assumptions that the adherends deform in a linear elastic manner, which may not be valid with increasingly tougher adhesives, as plasticity in the adherends becomes more likely. Thicker adherends are often used to reduce or prevent adherend plasticity, however the use of thicker specimens raises concerns with the accuracy of slender beam theory, often assumed in the data analysis methods for determining fracture energies. Increasing specimen length to allow for longer specimens and precracks to circumvent this issue may not be practical in available test frames and environmental chambers. Furthermore, as the contributions from the mode II component of the applied energy release rate increases, the fracture efficiency is reduced [45], meaning that the non-singular bending stresses in the adherends increase with increasing mode mixity. Loading fixtures, such as for MMB tests, may need to be redesigned to handle higher loads necessary for testing tougher adhesive systems as well. So, though numerous test methods have been proposed and used to characterize adhesive fracture behavior, high toughness adhesives pose increasing challenges for meaningful fracture energy characterization.

A popular approach employed by engineers to validate material properties and simulate the performance of adhesive joints is the cohesive zone model (CZM), which is now available in most commercial finite element codes. CZMs trace their origin to the works of Dugdale [46] and Barenblatt [47] to describe the stresses in the inelastic region ahead of a crack tip. With the introduction of the finite element method, Hilleborg et al. [48] demonstrated how a CZM could describe the mode I fracture of concrete, using a model that accumulates damage when extended beyond the displacement corresponding to the designated maximum traction. A cohesive element serves as an analog to the strength of a bond, prescribing tractions between continuum elements displaced by opening or sliding. This relationship between traction and displacement is known as the traction separation law (TSL) of the element. A CZM that needs to cover a range of loading scenarios, often mixed-mode I/II loading, will typically utilize two TSLs for the pure modes, a coupled damage initiation condition, and a mixed-mode coupling law for propagation [37, 49, 50].

To acquire the material system properties required for a CZM analysis, one of three methods can be used: property identification[51], the direct approach[39, 42], and the indirect approach[52]. Property identification takes parameter inputs from specific tests meant to measure specific parameters, such as a bulk adhesive tensile test to acquire normal tractions and stiffness

and a thick adherend shear test to obtain shear tractions and stiffness. This approach is not the most robust, as tests used to collect data can be from either bulk specimens or bonded joints with varying adhesive layer thicknesses; this is to say that the varying levels of constraint imposed on the adhesive by different specimen geometries are understood to give different apparent strength and fracture values, lower than the true traction limitations. The direct approach is performed by running fracture test, like a DCB or ENF specimen, and taking the derivative of a plot of G_c versus the crack mouth opening displacement (CMOD) of the adhesive layer, to acquire the TSL. The advantage of this method is that, by directly acquiring a TSL, one acquires tractions as a function of displacement. The inverse approach employs a curve fitting technique, often iterating through CZM parameters to optimize a fit between load versus crosshead or crack-mouth opening displacement curves. Both the property identification and indirect techniques require the user to pre-select the shape of the CZM. The choice of approach often depends on what information is available, but many researchers like the direct approach because all of the necessary parameters for a TSL can be directly extracted through derivation of the G_c with respect to the displacement of the mode. This method has become increasingly popular, providing additional insights and support for proposed shapes of TSLs, and much work has been done to define shapes of TSLs for different materials. Commonly employed CZM shapes are the constant stress, bilinear, trapezoidal, exponential, and polynomial forms. Bilinear TSLs are triangular in shape, with an increasing region of initial stiffness until the traction reaches its maximum value. After reaching this peak traction, the stiffness degrades until failure. The area under the curve is the fracture energy. The trapezoidal model is similar to the bilinear curve, but adds a yield plateau prior to the stiffness degrading until failure. Campilho et al. [53] explain that bilinear TSLs are a good model for mode I failures of most adhesives, whereas trapezoidal TSLs are better for modeling mode II fracture of ductile adhesives, which undergo significant plastic flow at near constant stress. Many researchers agree that the initial stiffness is not particularly important for a majority of bonded geometries and can be tweaked to improve convergence with little consequence [49].

To obtain TSLs, local measurements of displacement must be measured on each specimen. Digital image correlation (DIC) has emerged as the preeminent technique for measurement of local displacements, surface deformations, and rotations of test specimens. DIC is a non-contact, optical imaging technique that compares the relative movement of applied speckle patterns

to determine surface deformations. Recent works have used DIC on DCB tests to evaluate mode I TSLs, rate effects, and fracture process zone properties [54, 39, 42, 55, 41, 56]. Work using DIC to acquire mode II [57, 58] and mixed-mode I/II fracture properties [59, 60] of other adhesively bonded systems has been published, however the depth of this literature is sparse compared to mode I studies.

This paper demonstrates an approach that utilizes the DIC method and FEA to aid in the determination of a suitable mixed-mode I/II CZM for a recently developed epoxy-based structural adhesive, PR-2930 (PPG Industries, Inc), bonding 2024-T3 Al adherends. The utility and limitations of the conventional LEFM methods are discussed in the context of being used to analyze tough structural adhesive systems, such as PR-2930. A method for calibrating a mixed-mode I/II CZM model is described and its predictive capabilities for systems undergoing plastic deformations are subsequently shown. The CZM model is further validated when its load versus displacement predictions of a single lap joint (SLJ) geometry are compared to experimental results.

2. Experimental Methods

2.1. Specimen Fabrication

All specimens were fabricated using 2024-T3 Al adherends, with a thickness of 1.6 mm for SLJ specimens and 12.7, 19.1, or 25.4 mm for DCB, SLB, and ENF specimens. The range of thicknesses for the fracture specimens allowed for probing possible adherend plasticity and also preparing asymmetric specimens that offered slight variations from the mode mixity expected of the respective test method. Adherends were cut to size and the surfaces were grit-blasted by the fabricator. Surface preparation of as-received specimens followed instructions given by the manufacturer. The preparation required that the surfaces be (1) cleaned with acetone, (2) rinsed in deionized (DI) water for 2 minutes, (3) rinsed in an alkaline solution, CHEMKLEEN® 490MX (PPG Automotive OEM Coatings), recirculating at 49 °C for 2 minutes, (4) placed back in DI water for 2 minutes, and (5) dried in an oven at 60 °C between 10 and 30 minutes.

Upon removal from the oven, the adherends were allowed to cool to room temperature for about 10 minutes before application of the adhesive. Strips of polytetrafluoroethylene (PTFE) tape were placed on the bonding surface for each adherend to form a pre-crack. The location of the tape was dependent

on the test being conducted. Pre-crack lengths, a_p for DCB specimens were 75 mm; pre-crack lengths for SLB and ENF specimens were 107 mm from the roller supports to avoid propagation instability seen when $a_p < 0.7L$ [28]. These dimensions are shown in Figure 1. The PR-2930 adhesive was applied to substrates via a manual dispenser. Small glass spacer beads were incorporated into the as-formulated adhesive to maintain a bondline thickness of approximately 0.25 mm. Specimens were clamped in alignment and, per optimal cure recommendations for the adhesive, the specimens were placed in a convection oven set to 180 °C. SLJ specimens were cured for 10 minutes. Due to significantly greater adherend thicknesses relative to SLJ specimens, fracture specimens were cured for approximately 45 minutes to achieve bondline temperatures between 160-180 °C. Bondline temperature was monitored via a thermocouple placed in the bondline of a dummy specimen. After the desired cure time was reached, the oven was turned off and specimens were allowed to slowly cool in the oven overnight. PPG reported that aging of the adhesive was slow, so tests were conducted within 2 -14 days of specimen fabrication. Prior to testing, bondlines were coated with white spray paint to improve visibility of the crack tip. The crack tip progression was tracked with a paper ruler taped to the specimens starting at the pre-crack. For some selected specimens, neither the white spray paint nor the ruler were applied to the surface of the specimen and instead a speckle pattern was applied to the adherend surface for DIC analysis, as described in Section 2.4.

2.2. Specimen Geometries

Fracture specimen designations and their corresponding adherend thicknesses can be seen in Table 1, along with respective crosshead rates discussed in 2.3. Fracture specimen geometries and their relevant dimensions are given in Table 2. Figure 1 displays a schematic of the three fracture geometries and their dimension labels. SLJ adherend dimensions were nominally 1.6 mm thick, 25 mm wide, and 102 mm long with a 12.7 mm long overlap.

2.3. Specimen Testing

All tests were conducted at room temperature. SLJ and DCB specimens were tested in an Instron load frame (Norwood, MA) using either 5 kN or 30 kN load cells; the 5 kN load cell was used for 12.7S, 12.7A, and 19.1S DCB specimens, whereas the 30 kN load cell was used for 19.1A and 25.4S DCB specimens and all SLB, ENF, and SLJ specimens. Because specimens were of varying thickness, crosshead displacement rates varied from between

Table 1: Adherend pair designations with respective adherend thicknesses and test rates. For all specimens $B = 25$ mm.

Designation	h_1 (mm)	h_2 (mm)	Crosshead Rate (mm/min)
12.7S	12.7	12.7	1
12.7A	12.7	19.1	0.75
19.1S	19.1	19.1	0.5
19.1A	19.1	25.4	0.33
25.4S	25.4	25.4	0.25

Table 2: Fracture test geometries and dimensions.

Test Geometry	a_p (mm)	L (mm)
DCB	75	325
SLB	107	152
ENF	107	152

0.25 mm/min to 1 mm/min for fracture specimens[1]. Table 3 shows the number of tests that were conducted for each respective fracture geometry and designation.

Table 3: Number of specimens tested for each fracture test geometry.

Test Geometry	12.7S	12.7A	19.1S	19.1A	25.4S
DCB	4	5	5	5	3
SLB	3	3	4	3	2
ENF	2	–	2	1	–

The SLJ specimens were displaced at a crosshead rate of 1.3 mm/min per ASTM D1002-10 [63] and tested until complete separation of the adherends occurred. Approximately 25 mm of each end of the SLJ specimens was placed in the wedge gripping fixtures. Load and crosshead displacement measurements were recorded by the software controlling the load frame. A

[1]Displacement rates were intended to be scaled based on compliance of each specimen, but respective thicknesses were erroneously squared rather than cubed, so scaling was in error by as much as a factor of two. Such small rate variations typically have limited effects in viscoelastic materials and these rates are in the range used by other rates seen in fracture testing literature for quasi-static conditions of similarly sized specimens [28, 61, 62] and did not appear to cause a significant difference in results

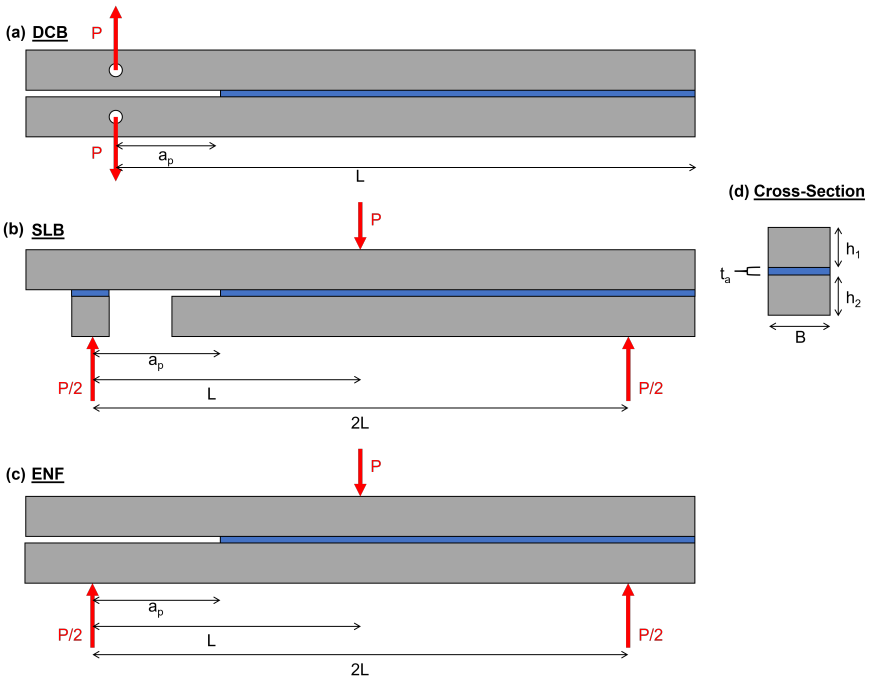

Figure 1: Configuration and dimensions for (a) double cantilever beam (DCB), (b) single leg bend(SLB), and (c) end notched flexure (ENF) tests, and (d) the cross section for these specimens. The exact dimensions can be found for a specific test and designation in Tables 1 and 2. Note the ENF tests has a bottom substrate identical to the top substrate.

total of 11 SLJ specimens were tested for this study.

A pair of SEIKA NA2-10 liquid capacitance inclinometers (RIEKER Inc; Aston, PA) with a measuring capacity of +/- 10 degrees were fixed to the free ends of the DCB adherends to measure end-rotations for determination of the mode I J-integral value via the Paris and Paris method [36, 40]. The inclinometers were fixed to each adherend via glued aluminum tabs placed at the ends of the adherends beyond the loading pins, as shown in Figure 2a. A DinoLite AM311 digital microscope (Dunwell Tech, Inc; Torrance, CA) was used to track and record the crack propagation. Crack length measurements were manually documented following the tests by reviewing digital microscope recordings. Crack tip propagation was often recorded about every 3-5 mm, however this was not always possible due to occasional difficulties in locating the apparent crack tip. Crack tip length was recorded until it reached 250 mm of propagation beyond the pre-crack. Cracks beyond this

length typically would become unstable and rupture, presumably because of the fracture process zone reaching the edge of the specimen, possibly coupled with short beam attachment effects [64]. Tests were terminated when adherends completely separated and the fracture planes were then examined and documented.

SLB and ENF specimens were tested in an MTS load frame (Eden Prarie, MN) using a three-point bending fixture with a free span of 304 mm. An ENF specimen being loaded in this setup is shown in Figure 2b. Based on span and pre-crack length, cracks were ideally able to propagate 55 mm before test termination, however the center loading tup would interfere with the fracture process zone well prior to this. Tests were terminated after the crack tip arrested near the midspan loading point. Unlike DCB tests, SLB and ENF specimens do not separate because the bondline remains intact beyond the midspan. To separate these specimens to see the failure planes and capture scanning electron micrograph (SEM) images, drilled holes for loading pins placed on the uncracked edge were used to fracture the remainder of the specimen in a DCB mode.

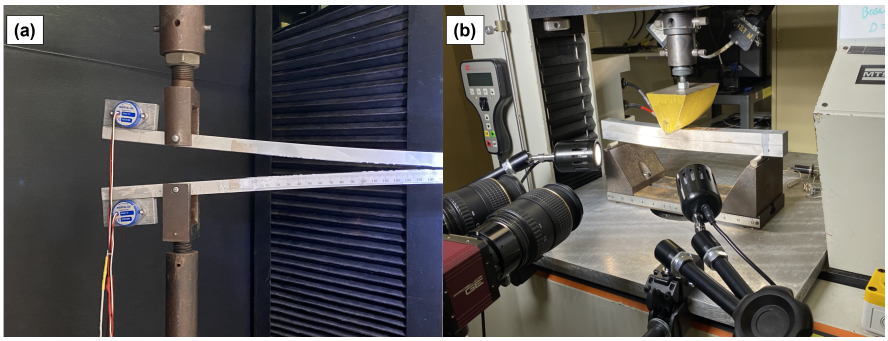

Figure 2: (a) A 12.7S DCB specimen with inclinometers fixed to free ends to measure rotation for determining J-integral and (b) a 19.1S ENF specimen with DIC being used to measure surface displacements from which strain fields could be obtained.

2.4. Digital Image Correlation

The DIC method was used to track surface deformations on the adherends, determine the strain fields in the plane of bending, and record crack propagation in the bondline for one of each type of test and geometry. The faces were randomly speckled with black spray paint using a perforated film under a fume hood. The black paint speckles were found to contrast well with

the metallic shine of the aluminum surface. White LED lights were arranged to properly illuminate the specimen and DIC cameras were set to capture the region of interest. Images were acquired with two Allied Vision Prosilica GE 4000 11 MegaPixel CCD cameras (4008 x 2672). The cameras were fixed to a tripod and offset by a calculated baseline distance, dependent on the desired field of view for the test. This arrangement is shown in Figure 2b.

Correlated Solution's (Irmo, SC) Vic Snap Image Acquisition software was used for calibration and imaging and its VIC-3D Digital Image Correlation software was used to perform DIC analysis. The sampling rate of images was determined depending on the test configuration and expected crack growth rate; DCB tests were sampled at a rate of 0.5 frames per second and SLB/ENF tests were sampled at 1 frame per second. In place of paper rulers used for visual determination of crack propagation, the high resolution DIC images were sufficient to track the propagation of the crack tip with analytical tools in VIC-3D employed to measure the location the crack tip. To verify the software's measurement of distances, small reference notches were machined 5 mm apart along the edge of the adherends. In a distance measurement calibration, the difference between DIC-measured distances and the notches was determined to be within 1%, and considered to be acceptable without adjustment.

In capturing the entire region of entire crack propagation, the regions selected for DIC analysis extended about 5-10 mm behind the pre-crack and 10 mm ahead of where the crack tip arrested. The subset size used for analysis was 55 x 55 pixels with a step size of 13 pixels. Analysis regions were placed on each adherend and not placed over the bondline, as the software could misconstrue crack opening as large deformation if the bondline was included in an analytical region.

3. Numerical Methods

3.1. Data-reduction Methods

Initial estimates of fracture energy were obtained through data-reduction methods and subsequently used in FEA modeling of fracture specimens to further calibrate the CZM properties of PR-2930. Mode I DCB tests were analyzed with the Corrected Beam Theory (CBT) [65], Compliance Based Beam Method (CBBM) [31], and the Paris and Paris J-integral Method [36].

Fracture energy calculated via the CBT method was taken as

$$G_{Ic} = \frac{6P^2(a+\widetilde{a})^2}{EB^2h^3} \tag{1}$$

where $\widetilde{a}$ is the crack length correction taken as the negative abscissa-intercept of the best linear fit of a plot of the cube root of compliance versus vs a data. P is the load acting on each adherend, E is the adherends' elastic modulus, h is the thickness of the (symmetric) adherends, and B is the adherend width. The CBBM method was used to determine fracture energy with the formula

$$G_{Ic} = \frac{6P^2}{B^2h}\left(\frac{2\widetilde{a}^2}{h^2E} + \frac{1}{5G}\right) \tag{2}$$

where the value $\widetilde{a}$ should be determined by a cubic root approach described in [31] and G is the shear modulus of the adherends.

The Paris and Paris $J - Integral$ approach is given as

$$J_{Ic} = P_w\theta \tag{3}$$

where P_w is the load per unit width and θ is the relative rotation between the two adherend ends at loading pin locations. This method must still follow the assumptions of the original J-integral derivation, two key assumptions of which are that the strains and rotations remain small.

3.2. Cohesive Zone Models

CZMs were simulated using the commercially available finite element software Abaqus (Dassault Systemes), which has built-in CZM modeling capabilities for bilinear, trapezoidal, and exponential shaped TSLs. Figure 3 shows the pure mode TSLs used in this study. Mode I TSLs were approximated by two bilinear models to explore fit. One model provided a better fit to load-displacement behavior at peak load and short crack lengths, while the other model fit better to the load-displacement behavior that was observed at longer crack lengths. For mode II, both a bilinear and trapezoidal cohesive zone shape were used. While the trapezoidal shape is reportedly more accurate for modeling the mode II behavior of ductile adhesives, Abaqus' built-in modules only allow for simple coupling of bilinear curves for mixed-mode fracture. Mixed-mode fracture with trapezoidal TSLs are often programmed as uncoupled models [2]. However, while difficult, this does not mean it is impossible to couple non-bilinear TSL shapes, as May et al. [66] used an adjusted mixed-mode fracture subroutine to predict the mixed-mode fracture

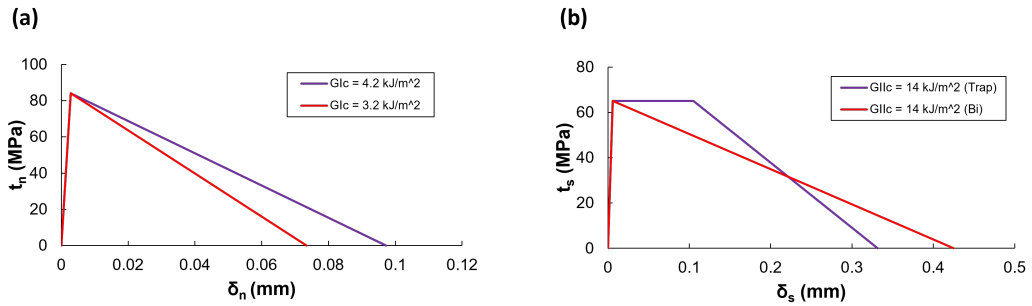

Figure 3: (a) Mode I TSLs used to model shorter crack lengths (purple) and longer crack lengths (red) and (b) trapezoidal (purple) and bilinear (red) shaped TSLs with equal fracture energies used for mode II to evaluate the fit and influence of TSL shape in the more ductile modes of failure.

toughness for the BETAMATE 1496 adhesive with a bilinear mode I TSL and trapezoidal mode II TSL. In this study, mixed-mode I/II fracture was approximated by coupling each of the two bilinear mode I TSLs with the bilinear mode II TSL. Like the pure mode TSLs, two models were used again to evaluate the fit of each for mixed-mode I/II fracture.

Damage initiation, the point where the initial TSL stiffness changes, was set to follow a quadratic nominal stress criterion given by

$$\left(\frac{\langle t_n \rangle}{t_{n,max}}\right)^2 + \left(\frac{t_s}{t_{s,max}}\right)^2 = 1 \tag{4}$$

where t_n and t_s represent the normal and shear tractions, respectively. The Macaulay brackets,$\langle\rangle$, signify that damage cannot be initiated by compressive stresses. When damage occurs, tractions are degraded by the following equation

$$t = (1 - D)\bar{t} \tag{5}$$

where $\bar{t}$ is the traction for a given displacement according to the initial stiffness and D is a scalar damage variable. D is 0 prior to the damage initiation and 1 at the failure of the element. A mixed-mode damage evolution law was simulated with the Benzeggagh and Kenane law [12] which defines the mixed-mode fracture energy as

$$G_c = G_{Ic} + G_{IIc} - G_{Ic}\left(\frac{G_{II}}{G_I + G_{II}}\right)^{\eta} \tag{6}$$

where G_c is the overall fracture energy for a given degree of mode mix, G_I and G_{II} are the respective mode I and mode II decomposed fracture energies for a given mode mix, G_{Ic} and G_{IIc} are the respective pure mode I and II fracture energies, and η is a fitting parameter. Simulations for mixed-mode specimens were performed with $\eta = 2$, as literature suggests this as a good fit for joints with aluminum adherends [67]. For the Benzeggagh and Kenane law, D evolves with each increment as a function of ratio of the total dissipated energy to the Benzeggagh and Kenane law determined G_c, similar to the power law damage evolution explained by De Moura et al. [68].

Table 4: Plastic properties of 2024-T3 Al used for Abaqus models.

σ (MPa)	Plastic Strain
324	0
340	0.0044
350	0.0081
380	0.0156
415	0.0276
460	0.0596
495	0.0956
540	0.1755

The 2024-T3 Al adherends were modeled with $E = 73.1$ GPa and a yield strength $\sigma_y = 324$ MPa. The plastic material properties, true stress and true plastic strain, used for the aluminum adherends are shown in Table 4. Initial stiffness and traction properties for PR-2930 were estimated from manufacturer-provided data. Their thick adherend shear tests on a 0.625 mm thick adhesive layer returned a shear modulus, G of about 1000 MPa and a shear strength of about $t_{s,max} = 65$ MPa. Uniaxial tension tests of the bulk adhesive were not performed because the exothermic nature of PR-2930 was deemed to preclude obtaining specimens of sufficient quality. Sugiman et al. [51] explained that when there is only a partial set of traction and stiffness data, one can apply an isotropic material relationship to acquire modulus and von Mises equivalence to obtain stress. Using the Poisson's ratio of a typical epoxy, $\nu = 0.35$, and applying the assumption of isotropism, the elastic modulus, E, was taken to be 2800 MPa. A combination of von Mises equivalence and manufacturer data gave an approximation of $t_{n,max} = 84$ MPa. These tensile properties were consistent with butt joint tests performed by the manufacturer [43]. Initial values of fracture energy,

G_{Ic} and G_{IIc}, were estimated from data-reduction analysis results, discussed in Section 3.1. The final values given for G_{Ic} and G_{IIc} were reached after iterations of FEA showed acceptable fits of the models to the data. All CZM properties are shown in Table 5.

3.3. Finite element analysis

Two-dimensional FEA models using plane-stress elements (CPS4) to model the adherends and cohesive elements (COH2D4) to model the adhesive layer were used. Yang and Thouless [61] have shown that plane-stress is optimal for defining adherends, as the softer adhesive layer does not provide the restraint required to achieve plane-strain conditions. The large thickness of the fracture adherends used herein would further substantiate this assumption. Element sizes for each model were 0.25 x 0.25 mm for SLB models and 0.5 x 0.5 mm for all other models. Due to the circular holes in the DCB model, the meshing could not produce just square elements, thus the 0.5 x 0.5 mm mesh size for the DCB models is a nominal size. All models used cohesive elements with a thickness of 0.25 mm and a length of either 0.05 mm for SLB models or 0.1 mm for all other models. This allowed for at least 10 cohesive elements to be present in all models' fracture process zone, as previous studies have recommended this is done for model optimization and convergence [69, 70]. A convergence study examined differences in P-δ output for 2 mm x 2 mm , 1 mm x 1 mm, and 0.5 mm x 0.5 mm adherend elements. Results for DCB and ENF specimens showed the difference in P_{max} was no greater than 1.25% between element sizes. Models were created and simulated for every experimental test and geometry. Figure 4 shows the boundary conditions and meshes for 12.7S DCB and ENF specimens.

Table 5: PR-2930 cohesive zone model parameters

E (MPa)	$t_{n,max}$ (MPa)	G_{Ic} (kJ/m$\hat{2}$)	G (MPa)	$t_{s,max}$ (MPa)	G_{IIc} (kJ/m$\hat{2}$)	η
2800	84	3.2 or 4.2	1000	65	14	2

4. Results and Discussion

4.1. Fracture Surfaces

Figure 5 shows the failure surfaces of symmetric (a) DCB, (b) SLB, and (c) ENF specimens as captured by camera and representative SEM images

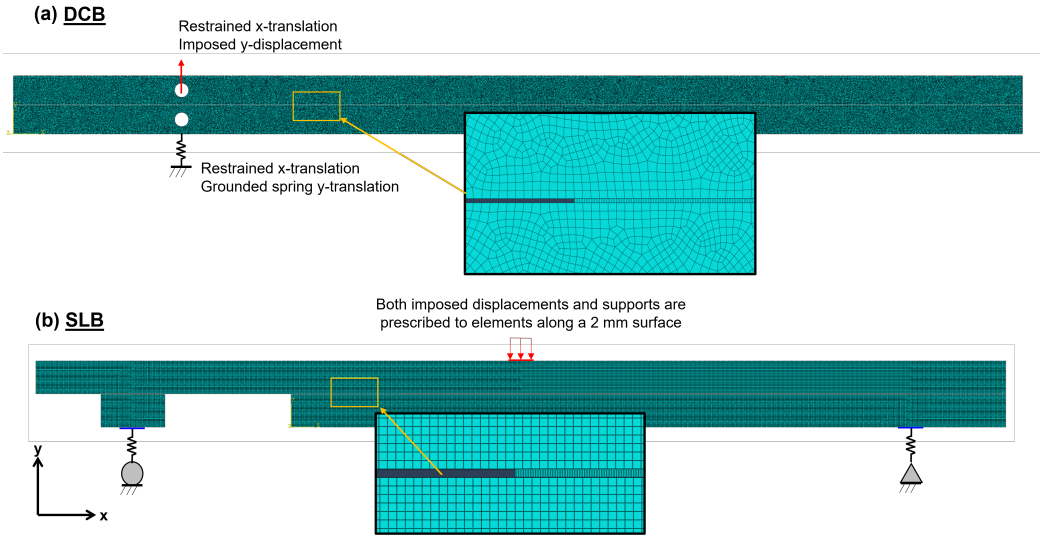

Figure 4: Finite element model boundary conditions and meshes for (a) 12.7S DCB specimen and (b) 12.7S ENF specimen. Spring boundary conditions were used at the supports to capture the load train compliance of the load frames used in experiments.

of the fracture surfaces. As mode mix shifts towards mode II, one will note the change of failure from cohesive fracture plateau patterns to hackle patterns [71] with failure visually appearing near the interface. As increasing amounts of compressive loading were placed, we suspect crack steering drove the adhesive to fail closer to the interface. The SEM images for the SLB and ENF specimens were taken from the surface of the adherend with more adhesive present (the lower adherend in the camera images). In SEM images of DCB and SLB failure surfaces, the presence of the spherical glass spacer beads is observed.

4.2. Data-Reduction Analysis

Figure 6a compares the mode I fracture energies, G_{Ic} versus the measured crack length, for these methods. The CBT and CBBM estimates of G_{Ic} are very similar, within about 3% of each other for each recorded data point. Compared to the CBT and CBBM methods, the Paris and Paris approach estimates a J_{Ic} that is significantly lower than the G_{Ic} values. Figure 6 shows G_{Ic} decreasing for about the first 75 mm of crack growth, followed by a "steady-state" region where the fracture energy appears to be relatively constant. This initial decline seems consistent among all DCB adherend

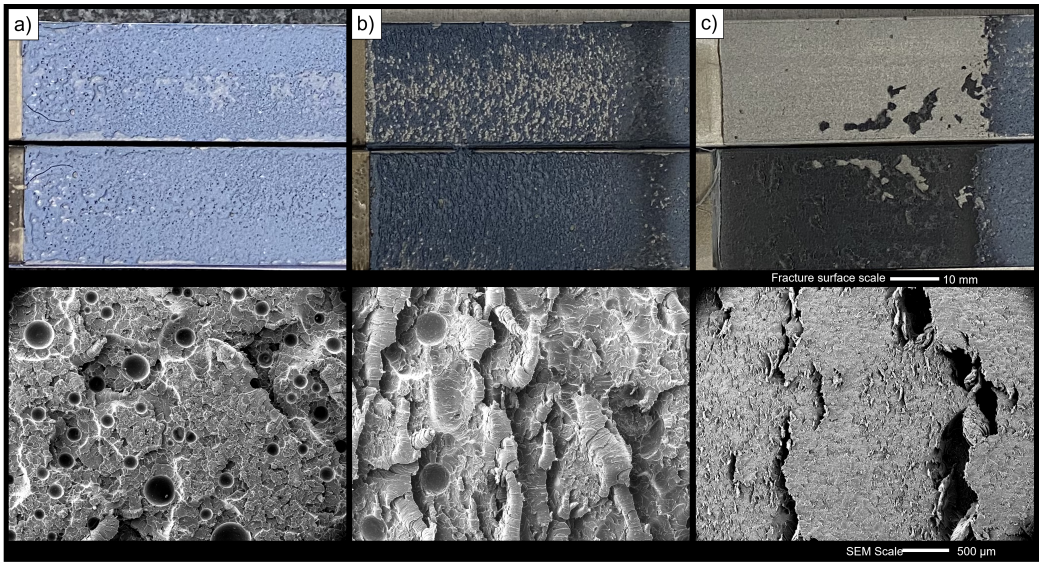

Figure 5: Camera and electron micrograph images for failure surfaces of (a) DCB, (b) SLB, and (c) ENF tests specimens.

thicknesses (see Appendix A) and analysis methods, though it is substantially smaller for the J-integral method.

Similar initial declines in G_{Ic} have been seen by others [72], and could arise from several sources. Decreasing values of fracture energy as a crack grows in DCB specimens has been seen for rate-dependent systems [73]. If the fracture energy was constant, one would expect the crack velocity to scale with a^{-1} at constant crosshead displacement rate. Some rate dependence is possible, though seems unlikely to be significant for this adhesive with a glass transition temperature of approximately 120 °C. Shear deformations in the adherends are present, and corrections, albeit imperfect [74], have been included in some analysis methods since the introduction of DCB specimens [8, 75]. Although not included in CBT, this contribution to compliance is considered in CBBM, and of course the J-integral method, which does not require an analytical approximation. The similarity of CBT and CBBM suggests this is not a significant factor for the 12.7 mm thick adherends, which, at the shortest (initial) crack length, would only amount to 1.7% increase in compliance, though rises to 6.9% for the 25.4 mm thick specimens. The blunt adhesive termination and lack of a sharp initial crack tip is a potential contributor to the initially declining G_{Ic} behavior, as a con-

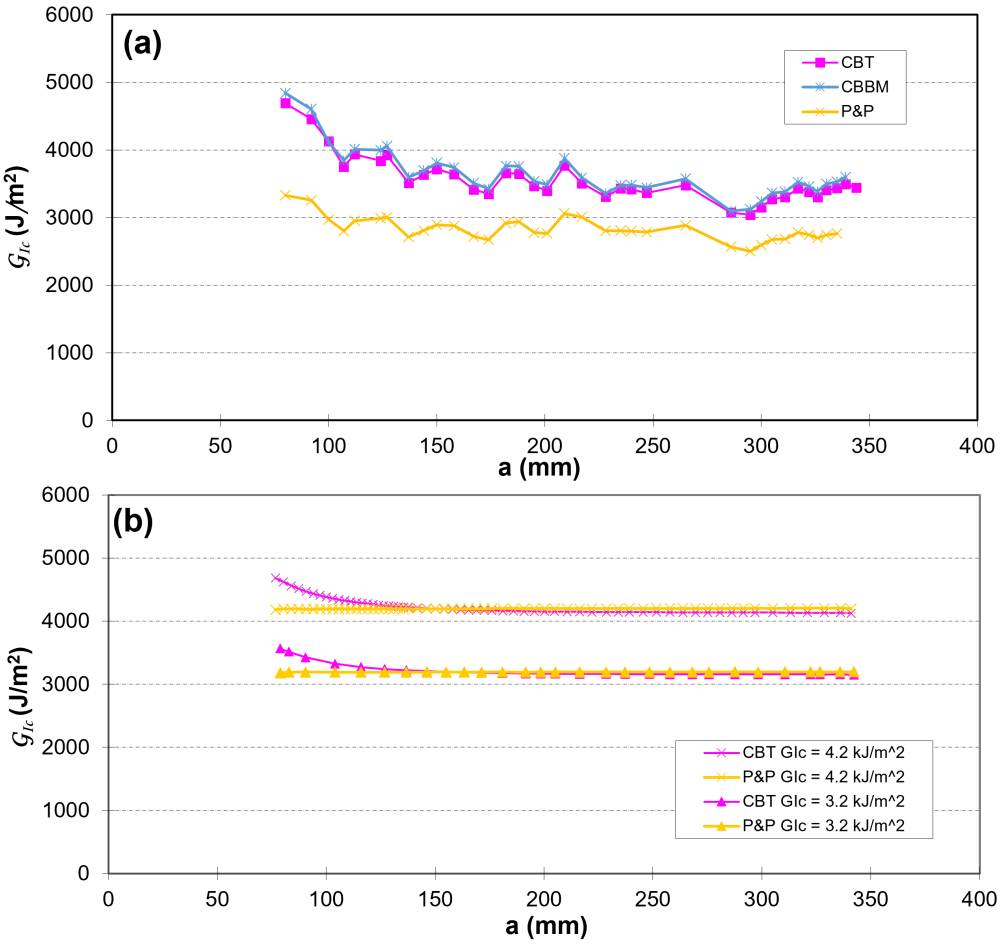

Figure 6: Fracture energy values versus crack length for a DCB-12.7S specimen, as determined by commonly used data reduction methods. (a) Data-reduction method fracture energies for experimental data and (b) data-reduction calculations of fracture energy using a 2D FEA model of a 12.7S DCB specimen.

sistent fracture process zone has not yet developed. However, if this was the dominant reason, one would expect to see similar decays for the J-integral analysis method. Such decays have not always been observed, even for tough and ductile adhesives [42, 41]. At short crack lengths, the higher applied loads result in an additional beam on elastic foundation (BoEF) compliance from root displacement that is not considered in the the CBT nor CBBM methods [74, 76]. Again, this would not be a limitation of the J-integral method, however. While the J-integral method would not be limited by considerable shear deformations, the inclinometers were placed beyond the ends of the loading pins because significance of shear deformations was assumed to be negligible. While for the thinner 12.7 mm DCB specimens, this assumption appears to be valid, for the larger 25.4 mm specimens this results in shear rotations not being captured and ultimately a more appreciable underprediction of J_c.

The CBT and CBBM G_{Ic} values are approximately 15-25% higher than J_{Ic}, as has often been seen by others [42, 41]. Whereas the CBT and CBBM calibrate for root rotation effects to obtain an effective crack length, these models assume that the adherend is traction free in the wake of the corrected crack length. Instead, substantial tractions are still involved for distances that include both the inelastic fracture process zone as well as what is assumed to be the elastic tensile region of the BoEF model. Sun and Blackman's study [41] showed these distances were on the order of the adherend thickness. These tractions thus reduce the DCB deflections compared to those modeled in the analytical approaches, leading to the difference between G_{Ic} and J_{Ic}. As the Paris and Paris method does not rely on an analytical model nor required assumptions, it is believed to be the more accurate approach for determining fracture energy. Interestingly, this method results in the most consistent value across the full range of crack lengths, not only for analyzing the experimental results, but also if used to extract the fracture energy from numerical simulations, as will be shown below.

Numerical analysis with finite element analysis (FEA) was used to gain additional insights into issues suggested above. Figure 6b illustrates results obtained by simulating the 12.7 mm thick behavior, then using simple beam theory CBT and the J-integral approach to analyze resulting displacement output. For these simulations, the model utilized input parameters for both mode I TSLs shown in Figure 3. Based on these assumed CZM properties, the J-integral method results in nearly a perfectly flat G_{Ic} of 3.2 kJ/m^2 and 4.2 kJ/m^2 for both FEA models, simulating a nearly perfect match with

the input value. The CBT results have a pronounced drop for G_{Ic} in the beginning, just like the experimental results for CBT and CBBM, however the CBT method plateaus around the model's input fracture energy. In light of this application of experimental data analysis methods to FEA output, we surmise that initial decays in CBT and CBBM are due to a combination of initiation from a blunt adhesive termination and the additional compliance resulting at shorter crack lengths from the BoEF contribution. The small initial decay from 3.3 kJ/m^2 to 2.9 kJ/m^2 shown for the J-integral method in Figure 6a, thus suggests the lack of a sharp crack, but the substantially larger decays in CBT and CBBM results are likely associated with the additional BoEF contribution from the higher applied forces at small crack lengths, as previously mentioned.

Mixed-mode SLB and Mode II ENF tests specimens using 12.7 mm and 19.1 mm thick adherends exhibited observable plastic deformation upon conclusion of testing. Due to the growing crack, it was unknown if the plasticity occurred around the pre-crack or if most of it accumulated as the crosshead continued to move after the arrest of the crack tip nearer the loading tup. Data-reduction methods used herein are strictly applicable only when LEFM conditions apply, thus due to plastic deformations these methods not able to obtain reliable results. While common data-reduction methods cannot easily resolve adherend plasticity, finite element analysis is a tool well suited to compute non-linear analyses. Despite this consideration, the ENF formulation for the CBBM [30] was used to estimate the mode II fracture energy, G_{IIc}, that was necessary for initial CZM inputs. Using data from a 12.7S and a 19.1S ENF specimen, the CBBM method estimated an average G_{IIc} of about 18 kJ/m^2. This value was understood to be higher than the actual G_{IIc} due to the greater compliance of plastically deforming specimens.

4.3. Finite Element Analysis

4.3.1. P-δ Curves

A common method for evaluating CZM properties involves fitting numerical P-δ curves to experimental P-δ curves. In the case where mixed-mode fracture envelopes are being developed, it is simpler practice to test the fit of TSLs for the pure modes first and then move to mixed-mode specimens to determine a suitable mixed-mode coupling relationship. All specimens were tested to failure except for the dotted gray curves on the P-δ plots, as these specimens were terminated early due to experimental constraints. FEA models were run until complete failure and many of the experimental curves

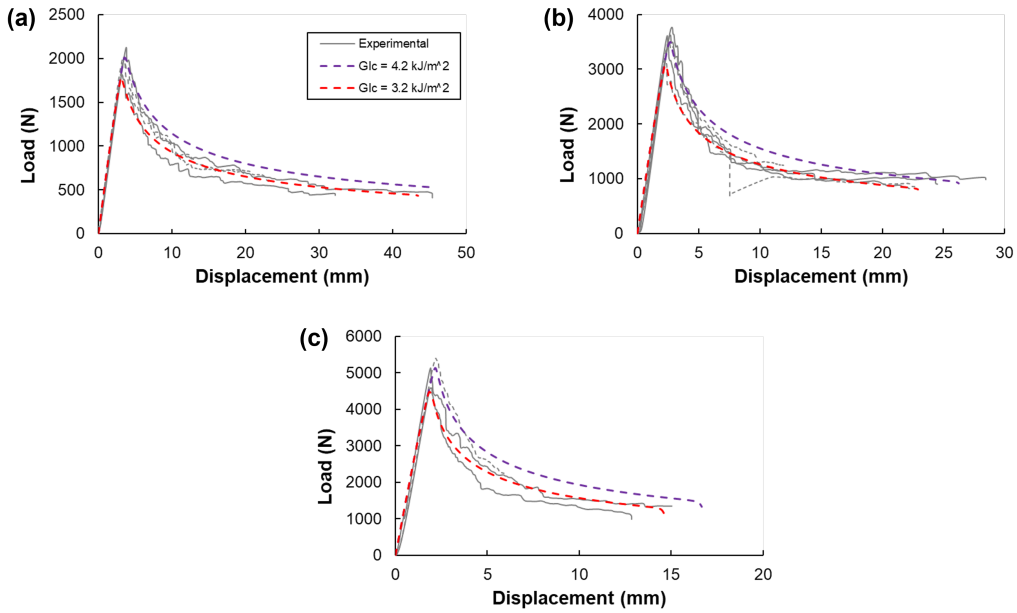

Figure 7: Load-displacement plots for the three symmetric DCB geometries along with predicted FEA results assuming either $G_{Ic} = 3.2$ kJ/m^2 or $G_{Ic} = 4.2$ kJ/m^2 for (a) 12.7S, (b) 19.1S, and (c) 25.4S DCB specimens. Such comparisons were used to guide calibration of mode I properties. As seen in these plots, while short crack lengths agree better with the $G_{Ic} = 4.2$ kJ/m^2 once the crack has become well-developed it tends to converge around $G_{Ic} = 3.2$ kJ/m^2.

show a failure displacement between the displacements given by the upper and lower bound TSLs that were used. The results from the DCB tests in Figure 7 show that the peak load and shorter length cracks are well fit by the $G_{Ic} = 4.2$ kJ/m^2 curve and as the crack grows, the fracture energy tends to converge to the lower bound of $G_{Ic} = 3.2$ kJ/m^2. While one may think the tractions would have greater influence on the peak value, it turns out because tougher adhesives result in large fracture process zones, the peak load is more significantly influenced by fracture energy. Additionally, while all the curves tend to converge at the lower bound, the upper bound of fracture energy is better at capturing the peak loads, which have much greater variance possibly due to differences in the exact lengths and crack profile of the initial flaws.

ENF results show that the TSL model using mode II fracture energy of 14 kJ/m^2 fits well to the P-δ curve. This value was reached by iterating

through fits of mode II fracture energies starting with the value of 18 kJ/m^2 acquired in Section 3.1. For the smaller 12.7S ENF specimen, both the bilinear and trapezoidal curves produce very similar P-δ responses to the experimental data. The larger 19.1S ENF specimen appears to be more sensitive response to TSL shape, as the bilinear curve has a much more rapid stiffness degradation due to the immediate decline of tractions in the TSL. This is consistent with Alfano's study [77] showing stiffer adherends increase cohesive zone length and in turn, the shape of the TSL becomes more influential on the model's results.

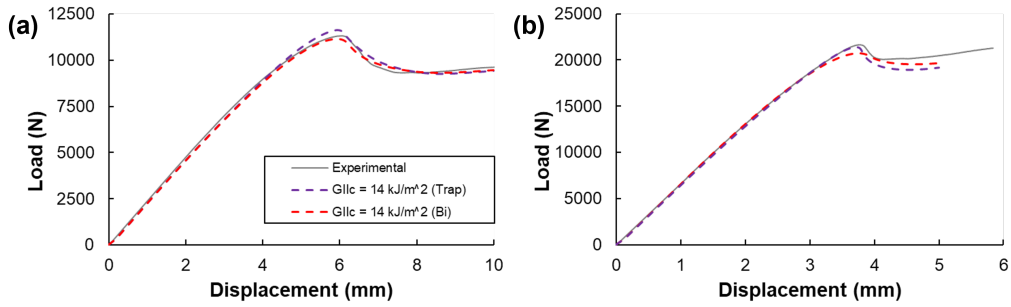

Figure 8: Experimental and FEA load-displacement plots for two ENF geometries: (a) 12.7S (b) 19.1S ENF. Both FEA models used $G_{IIc} = 14$ kJ/m^2, but one model used a bilinear TSL and the other used a trapezoidal TSL, the former being less computationally expensive and the latter having been shown to be more accurate for modeling mode II TSLs [53]

Mixed-mode specimens evaluated the fits of both mode I TSLs with the bilinear mode II curve with $G_{IIc} = 14$ kJ/m^2 being used for simplified coupling. Figure 9 shows the load displacement response of (a) a 12.7A DCB specimen, (b) a 19.1S SLB specimen, and (c) a 19.1A SLB specimen. While the fracture energies agree better with lower $G_{Ic} = 3.2$ kJ/m^2 for the 12.7A DCB specimens, the SLB specimens agree better with $G_{Ic} = 4.2$ kJ/m^2. The difference in optimal fits of G_{Ic} may be best described by the large difference in allowable crack propagation between the two tests. SLB and ENF specimens had only approximately 35 mm of crack propagation before the crack tip arrested. This may have been due the fracture process zone entering a region with a more complex stress state arising from the nearby loading tup. At a crosshead displacement of 5-6 mm, the 12.7A DCB specimens in Figure 9a have an approximate crack propagation of 35 mm. This may suggest a reason why SLB and ENF data agree better with the larger fracture energy of

$G_{IIc} = 4.2$ kJ/m^2. The apparent drop in G_{Ic} as the initial crack propagates may be due an anomalous fracture process zone that is more dissipative in the initial stages of crack growth when loads are greater and the crack tip is developing.

Using the same tests with longer span or other tests such as the fixed-ratio mixed mode (FRMM) or End Load split (ELS) would be recommended for acquiring data regarding mode II fracture with a more fully developed fracture process zone. For the 304 mm freespan ENF and SLB specimens tested in this study, the loading tup was only 45 mm from the precrack, giving some concerns about the relatively short distances within which the fracture zone evolves.

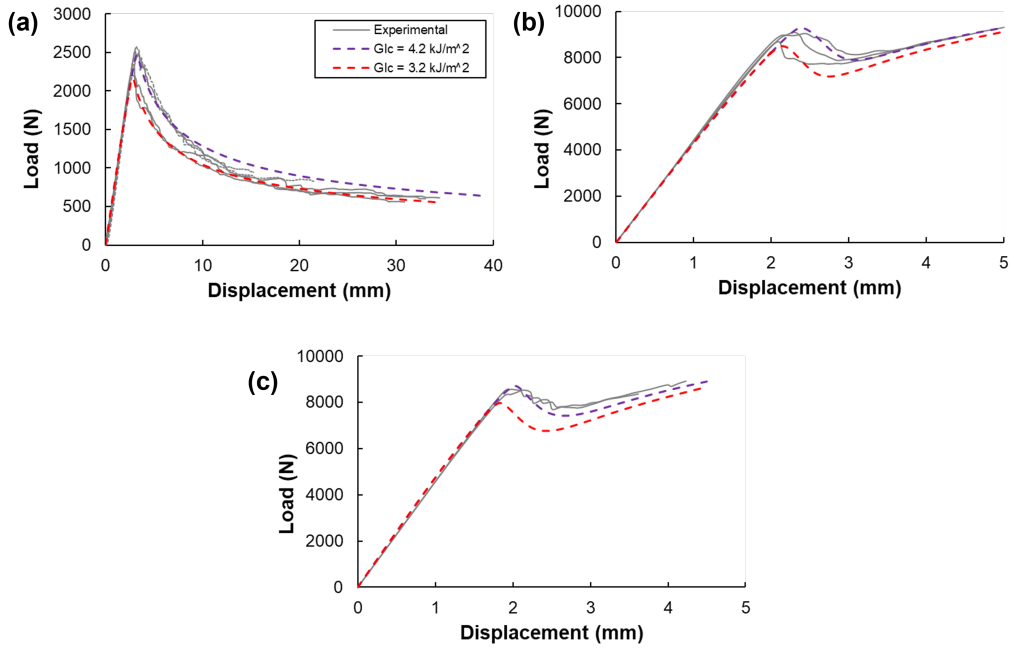

Figure 9: Experimental and FEA load-displacement plots (a) 12.7A DCB, (b) 19.1S SLB, and (c) 19.1A SLB curves used to calibrate mixed-mode I/II relationship.

4.3.2. Local measurements with DIC

P-δ curves provide essential global behavior needed to extract fracture parameters, but other methods are necessary to capture local deformations, such as around the crack tip. These local deformations provide deeper insights to the interactions between the adhesive and the adherends, like more

precise details on the TSL and limitations of the model. Using DIC, experimentally measured local displacements (aka CMOD) and strains were compared to simulated CZM results as loading proceeded. Local displacements were measured by taking the displacement differences between CMOD inspection points about 2 mm above and below the interface at the pre-crack. Figure 10 shows the location of these local displacement measurement points and one strain interrogation point for both a DIC strain field of a 12.7S DCB specimen and the corresponding region of the FEA model. Taking local displacement measurements at the pre-crack location allowed for the elimination of machine compliance and any rigid body motion. Strains were also measured at the same height above the bondline, but at points further ahead of the pre-crack (75 mm for DCB specimens and 20 mm for SLB and ENF specimens), as the measurements of strain at the pre-crack were often erratic. Strain results at the pre-crack may have been spurious due to significant differences in stiffness between the unbonded and bonded regions and the influence of neighboring subsets on the smoothing algorithm used to determine strain. Gorman and Thouless [39] have noted the greater compliance of the adhesive compared to adherends can also confound data when subsets contain both materials. While not performed in this study, bondline deformation prior to crack growth could be measured if a small enough speckle pattern was applied to the bondline, such as what has been shown by [37, 56, 78]. Furthermore, strains further away from the pre-crack were of interest because of our assessment that the fracture process zone was more fully-developed and consistent away from the pre-crack. The DIC-acquired strains were directly compared to strains measured within elements at similar locations in the finite element CZMs.

Figure 11a plots the load against the local displacement for a 12.7S DCB, which was calculated by taking the difference between the displacement of the local displacement interrogation points . The plot only shows the first 1 mm of local displacement, however the total local displacement went up to about 13 mm (corresponding to 23 mm of crosshead displacement) until the test was terminated due to the bounds of the DIC imaging frame being reached. Only 1 mm of the local displacement is shown in Figure 11a to convey how the experimental data initially matches the peak load of the $G_{Ic} = 4.2$ kJ/m^2 curve, but quickly descends toward the lower bound of $G_{Ic} = 3.2$ kJ/m^2. Strain measurements shown in Figure 11b and Figure 11c show the measured longitudinal strain,ϵ_{xx}, at pre-crack and 75 mm away from the pre-crack. The difference in the fracture energy models shown in

both figures gives credence to the idea that the initial fracture process zone dissipates more energy compared to the one that develops as the crack starts to grow in a steady-state fashion. Part of this could likely be attributed to the lack of a sharp pre-crack, as well as the significant lateral loads coupled with the moment at the crack tip. The local-displacement shows that as soon as the pre-crack propagates, the fracture energy quickly approaches the lower value. The initial stiffness of the mode I specimen degrades much more quickly prior to peak load in the numerical models. This is of little consequence regardless, because the $G_{Ic} = 3.2$ kJ/m^2 models provide good fits to the rest of the data.

Figure 11d shows the agreement between FEA and DIC-measured transverse strains, ϵ_{yy}, taken from a point 75 mm in front of the pre-crack. Both the experimental and numerical data show the classical beam on elastic foundation (BoEF) model [79] that has long been used to describe the stresses and deformations of beams on complaint foundations [80]. This analysis has been shown to still be valid with tough adhesives for analysis of even the most ductile adhesive joints [41]. Interestingly, the ϵ_{yy} strains from the specimen surface captured by DIC are shifted downward to become more compressive compared to the FEA strains. This may be due to anticlastic bending effects which are most extreme on the edges of the 25 mm wide specimen, but not captured in 2D plane-stress FEA models.

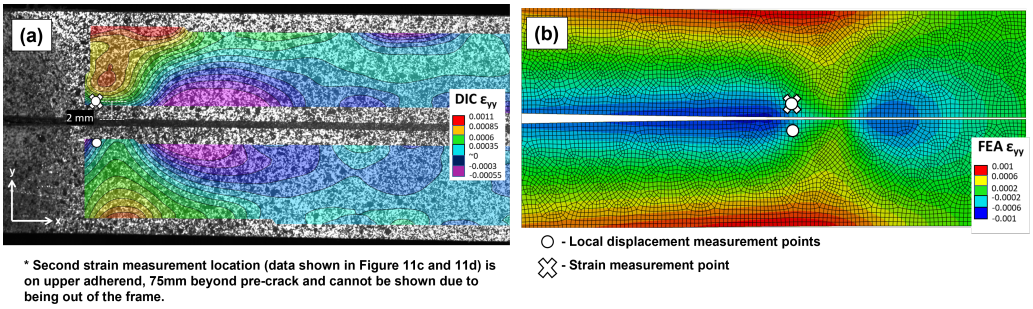

Figure 10: (a) DIC and (b) FEA strain fields for a 12.7S DCB specimen. The white circles mark the locations used to find the CMOD of specimens. For the DCB specimens, strains were considered in the upper adherends at both the local displacement point and another point not in the frame, 75 mm beyond the pre-crack.

Figure 12 shows the strain fields just prior to crack propogation for 12.7S ENF model recorded by DIC and simulated by FEA. The local displacement and strain measurement points are marked on the figure. Mode II local

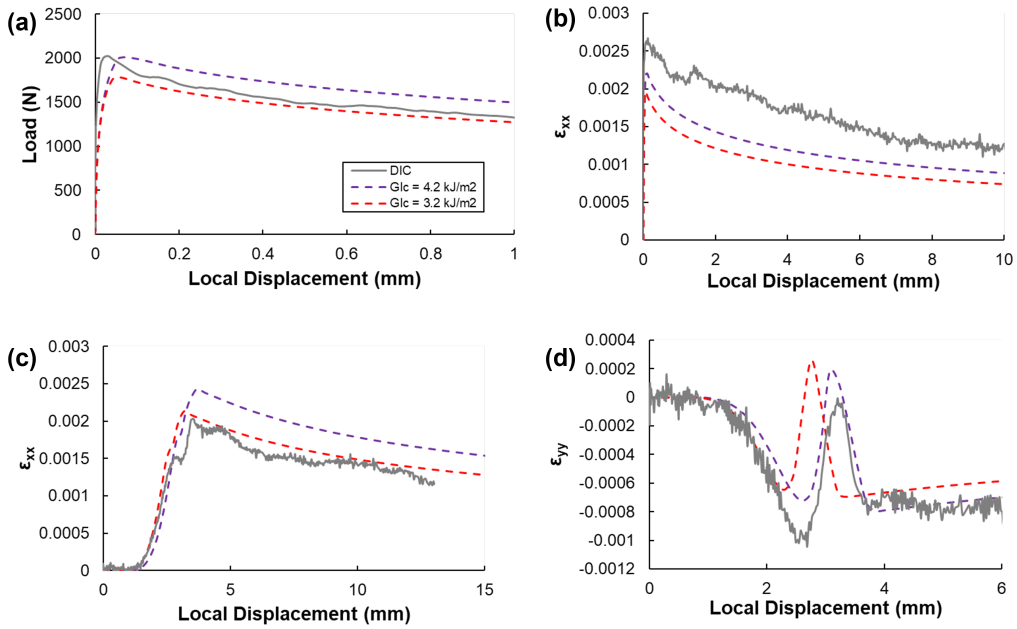

Figure 11: Load and strain components as functions of CMOD for a 12.7S DCB specimen (a) Load versus Local Displacement, (b) ϵ_{xx} at pre-crack, (c) ϵ_{xx} 75 mm from the pre-crack, and (d) ϵ_{yy} 75 mm from the pre-crack

displacement data highlights the effects of the two different TSL shapes on the specimen's deformation response. The data shown in Figure 13 is for the 12.7S ENF specimen whose P-δ response is shown in Figure 8a. The P-δ response of this specimen does not show a significant dependence on TSL shape, however when using more localized data it becomes apparent that a bilinear model is not as accurate as the trapezoidal model. As observed with the P-δ curve in Figure 8b, the trapezoidal model in Figure 13a provides an improved fit to the DIC-measured local sliding displacement compared to the bilinear model. Plots of ϵ_{xx} and ϵ_{yy} versus load are shown in Figure 13b and c. Unlike for mode I, the strain imposed on the adherends is driven by shear tractions corresponding to ϵ_{xx}, with ϵ_{yy} largely being driven by Poisson's effect instead of normal tractions. Interestingly, the initial slopes of both strains have opposite signs than expected, however the magnitudes of the strains are quite small and may be due to Poisson's effect.

DIC was used to obtain local opening and sliding displacements at the pre-crack for a 12.7S SLB specimen. As the DCB and ENF tests provided

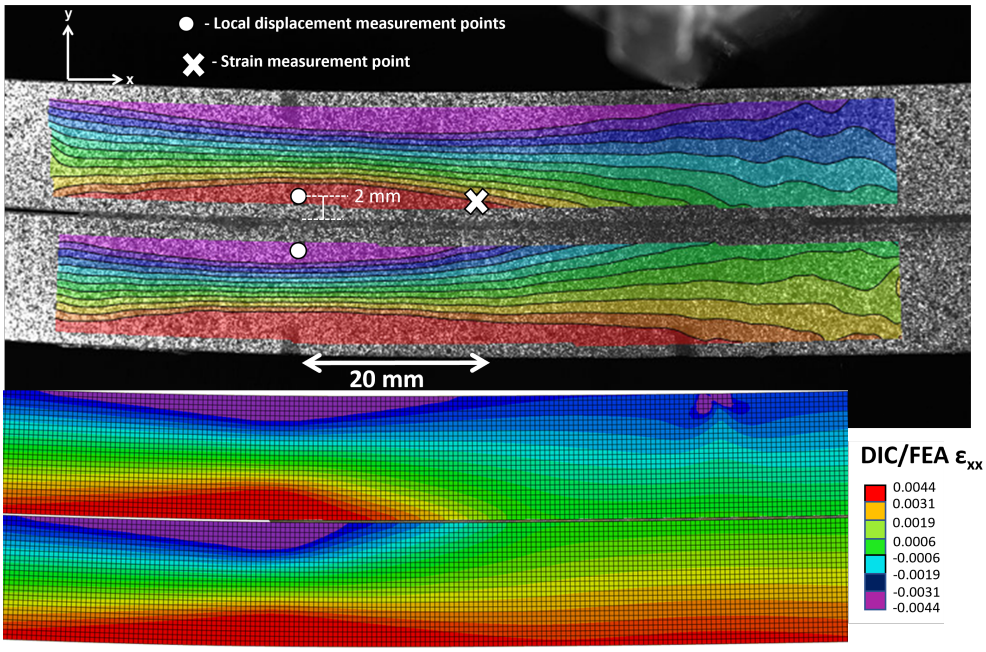

Figure 12: (a) DIC and (b) FEA strain fields for a 12.7S ENF specimen just prior to crack propagation. The white circles mark the locations used to find the local displacements of specimens and the x marks the strain measurement points. The scale bar in this figure is set to a maximum strain of 0.0044, which is the approximate uniaxial yield strain of 2024-T3 Al.

good insights into pure mode I and II TSLs, the SLB and asymmetric geometries could be used to evaluate the fit of the Benzeggagh-Kenane coupling law used to complete the mixed-mode fracture envelope for the tested specimens. The DIC and FEA strain fields as well as the load versus opening and sliding displacements are shown in Figure 14. While some refinement of the coupling parameter, η, could be made to get better agreement between the failure of both modes, this is not necessary as the combination of the load versus local displacement curves in Figure 14 and global P-δ curves in Figure 9 show strong capacity of the CZM parameters used to model the mixed-mode behavior. This is very important, as mixed-mode fracture is the most practical form of failure in bonded materials and the capabilities of finite element analysis to be able to capture such fine local effects in mixed-mode fractures is impressive.

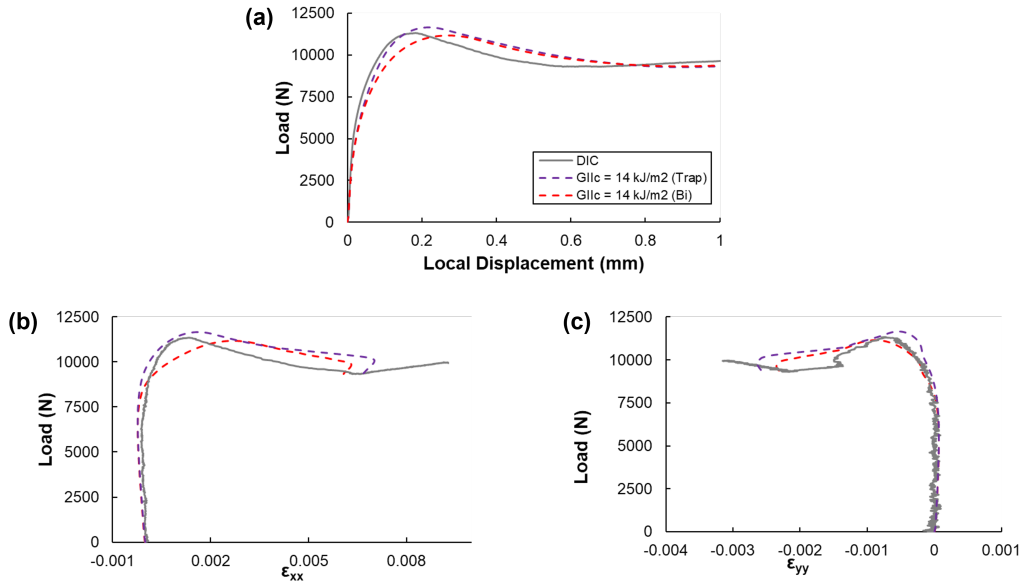

Figure 13: Plots of load vs local displacement results from DIC analysis of ENF specimen. (a) Load versus local sliding displacement, (b) ϵ_{xx} at pre-crack, (c) ϵ_{xx} 75 mm from the pre-crack, and (d) ϵ_{yy} 75 mm ahead of the pre-crack for the ENF 12.7S specimen

4.4. Model Transmissibility

There have been numerous studies that show the fit of a CZM is dependent on the material and geometric properties of both the adhesive and the adherend, such as those by Campilho and Banea et al. [53, 81]. For engineering design, however, constraints of time and expenses result in an approach where an adhesive's mechanical properties are identified through tests of a limited set of joint configurations (i.e. bondline thickness, adherend materials, adherend dimensions,) and these properties are then used to predict behavior of other bonded joint configurations. Sections 4.3.1 and 4.3.2 show how the calibrated CZM models were able to model the response of a variety of specimen adherend thicknesses for several loading scenarios. The 25.4 mm adherend geometry is approximately 8 times stiffer in bending than the 12.7 mm specimen, and the ability of the chosen CZM models and parameters to accurately represent the range of cases suggests good transmissibility of the model, at least for the given experimental load cases. However, this is a relatively simple and idealized example of the configurational transmissibility. The utility of the models was further demonstrated by modeling a very different geometry – the single-lap joint (SLJ) test.

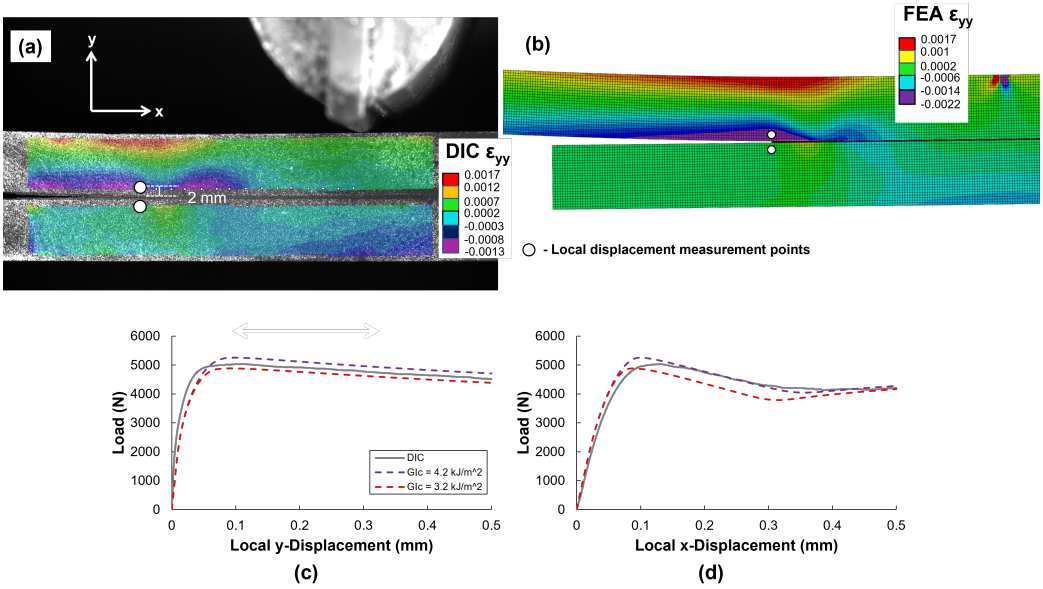

Figure 14: (a) DIC and (b) FEA strain fields for a 12.7S SLB specimen and the corresponding plots for (c) load versus local y-displacement and (d) load versus local x-displacement for the specimen.

The SLJ, described by ASTM D1002-10 [63], is one of the most widely used methods in industry for testing and comparing structural adhesives. The SLJs are described in the ASTM standard as a test for measuring the "apparent shear strength", but often the large peel stresses occurring at the terminal edges of the joint are the primary mechanism responsible for precipitating failure [82]. Although various analytical models for SLJs have been proposed, FEA would be the more general approach, allowing one to analyze stress states in this and more complex configurations.

Figure 15a shows the mesh and dimensions of the FEA models used to simulate the SLJ test. The SLJ model used the same adherend and cohesive zone material inputs as the fracture specimen models discussed in section 3.2. As a strength test rather than a fracture test, SLJs typically do not contain intentional initial flaws. Due to this, the 4.2 kJ/m^2 mode I fracture energy was expected to be the more appropriate CZM model for SLJ specimens, however both this and the 3.2 kJ/m^2 model results are shown in Figure 15d and a roller on the end of the applied displacement corresponding to the moving crosshead. The boundary conditions and mesh of the model are shown in

Figure 15a. The load versus displacement response between the model and the experimental DIC showed a good predictive response, especially when one considers the initial experimental compliance due to the gripping action between the fixtures and adherends. It should be noted, varying mode II fracture energy does not significantly influence load-displacement response of a SLJ model [83]; this combined with the consideration that there are many parameters input to a CZM may help future researchers understand that the SLJ test is better for validating CZM parameters as opposed to being used for calibrating the parameters for a mixed-mode CZM.

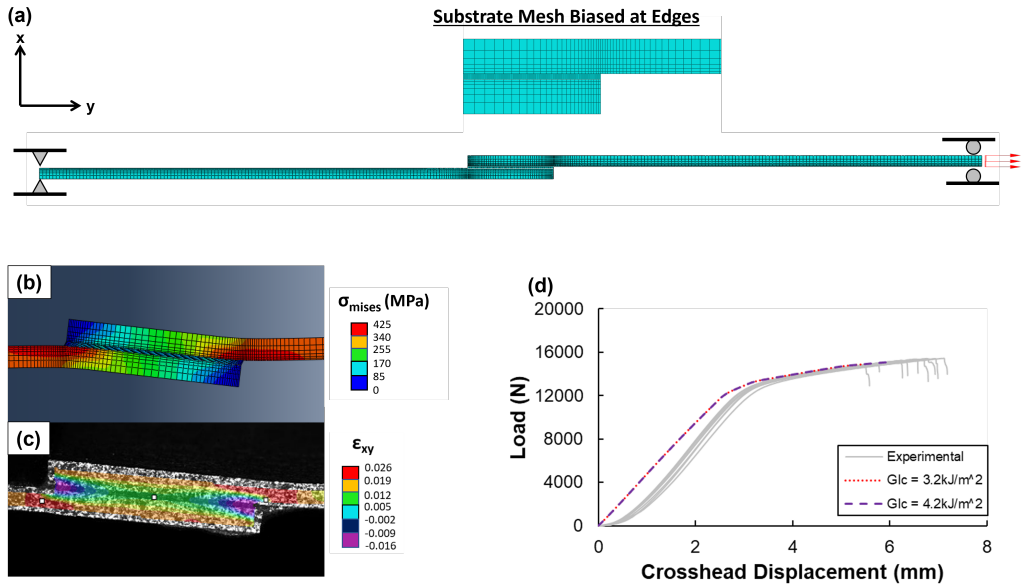

Figure 15: (a) FEA mesh and boundary conditions for SLJ model, (b) von Mises stress at bonded area for SLJ FEA model, (c) shear strains measured in experimental specimen with DIC, and (d) load-displacement response of the FEA models versus experimental results from a set of SLJ specimens.

5. Conclusions

This study served to explore commonly used experimental and numerical techniques to characterize the mechanical properties of the PR-2930 adhesive bonded to 2024-T3 Al adherends. Popular experimental fracture geometries were tested to provide data for pure mode I and mode II fracture and the mixed mode I/II region too. As slight amounts of adherend plasticity were

observed in pilot DCB specimens, and larger amounts of plasticity were observed in ADCB, SLB and ENF, more advanced methods of data acquisition were introduced. The DIC method was found to provide useful qualitative and quantitative displacement and strain measurements, which could be evaluated against simulated FEA models to evaluate various adhesive TSLs.

Poor agreement between data-reduction methods such as the CBT, CBBM, and the J-integral in mode I tests in addition to the occurrence of plasticity in ADCB, SLB, and ENF tests necessitated the use of more advanced numerical analysis, FEA, to determine the mixed-mode fracture envelope for the 2024-T3 Al joints bonded by PR-2930. Using cohesive elements to simulate the adhesive, a good fit of constitutive properties to describe the strength and toughness was found for the PR-2930 adhesive. A bilinear mode I TSL with a fracture energy of about 3.2 kJ/m^2 was found to fit DCB data well, and a trapezoidal TSL with a fracture energy of about 14 kJ/m^2 was found to predict ENFs load-displacement response sufficiently. While the TSL shape for such a tough adhesive like PR-2930 becomes more trapezoidal in shape as mode II contributions increase, it was determined that even less-ideal bilinear coupled-TSL still provided good agreement with the data from mixed-mode tests. Using empirical equations 4 and 6 to interpolate mixed-mode TSLs was found to provide acceptable fits to the data. If one were to model bonded joint geometries with less stiff adherends, when details of the the TSL become more significant, these equations may prove to be more limiting for fitting data. The CZM model acquired was then compared to load-displacement results from experimental SLJ tests and shown to provide good agreement. CZMs in commercial FEA packages would be improved for modelling similar structural adhesives if commercial software provided a coupled CZM input allowing for the shape of the TSL to become more trapezoidal as the mode mix shifts to more mode II contributions.

Due to the tolerance for plastic deformations in this study, the techniques demonstrated are well suited for industrial applications where there is typically less of a need to preserve resources and material supplies compared to academia. Furthermore, the use of pre-existing models in commercially available FEA software provides the advantage of saving time in lieu of to developing more complex analytical models to be used by the software.

With development of increasingly tougher adhesive formulations, thicker adherends will be needed to avoid adherend yielding in common fracture test geometries. The effects of 'short' beam geometries and of the large shear forces required at short crack lengths were discussed in light of their direct

relevance, suggesting the need for further consideration and inclusion. Shear deformation becomes more significant when long, slender beam bending assumptions become less applicable for thicker adherends, especially at initially short (e.g. $a/h < 10$) crack lengths. In addition to these shear deformation concerns, thicker adherends also may lead to short BoEF effects for shorter bonded ligaments (e.g. $(L-a)/h < 10$ for the DCB specimen [64]) and also broadening of the affected zone near the loading tup for ENF and SLB specimens.

This study demonstrated the utility of combining cohesive zone models in finite element packages with DIC for data acquisition. As structural materials become tougher to keep up with the demands of engineering, the need to have sufficient tests and methods of data extraction increases. Similarly, with continuous improvements in computational power, the use of more powerful numerical solvers can allow for better predictive capabilities and insights into the limitations of underlying analytical models.

6. Acknowledgments

The authors would like to thank Marvin Pollum for significant advice on fabricating specimens, and Profs. Kenneth Liechti, Bamber Blackman, and Michael Thouless for helpful insights. CMJ was supported by the Department of Defense (DoD) through the National Defense Science and Engineering Graduate (NDSEG) Fellowship Program. We acknowledge the Virginia Tech Macromolecules Innovation Institute for fostering interdisciplinary studies in adhesion, and for travel support to disseminate this work. This work was performed in part at the Nanoscale Characterization and Fabrication Laboratory, which is supported by the Virginia Tech National Center for Earth and Environmental Nanotechnology Infrastructure (NanoEarth), a member of the National Nanotechnology Coordinated Infrastructure (NNCI), supported by NSF (ECCS 1542100 and ECCS 2025151). This material is based upon work supported by the National Science Foundation under OISE Grant No. 1854185. PPG Industries, Inc. acknowledges that research was sponsored by the U.S. Department of Defense and was accomplished under Cooperative Agreement Award HQ0034-15-2-0007 to NCMS. The views and conclusions contained in this report are those of the authors and should not be interpreted as representing the official policies, either expressed or implied, of the U.S. Government. The U.S. Government is authorized to reproduce and distribute reprints for Government purposes notwithstanding any copy-

right notation herein. All third party trademarks and company names are the property of their respective owners.

Appendix A. Appendix A: Results for all DCB adherend thicknesses

Figure A.16 compiles CBT-determined G_{Ic} for all symmetric DCB tests. Much of the data lies within 20% above and below an average of about 3 kJ/m^2. Similarly, Figure A.17 compiles Paris and Paris J-Integral determined J_{Ic} for most of the symmetric DCB tests. Again, much of the data lies within 15% above and below an average of about 2400 kJ/m^2. No clear trend is apparent across the three symmetric thicknesses used, and no obvious adherend plasticity was observed for any of these specimens. All CBT and J-Integral results showed a decline from about 75 mm to 150 mm, which is more obvious for the CBT data and likely due to reasons discussed in the paper.

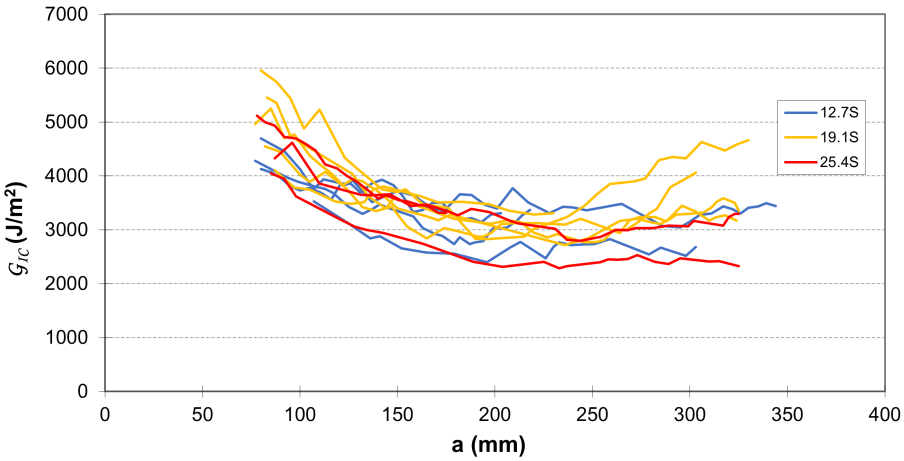

Figure A.16: CBT-calculated fracture energy vs measured crack length plot for all DCB specimens.

References

[1] S. Hashemi, A. J. Kinloch, J. Williams, The analysis of interlaminar fracture in uniaxial fibre-polymer composites, Proceedings of the Royal

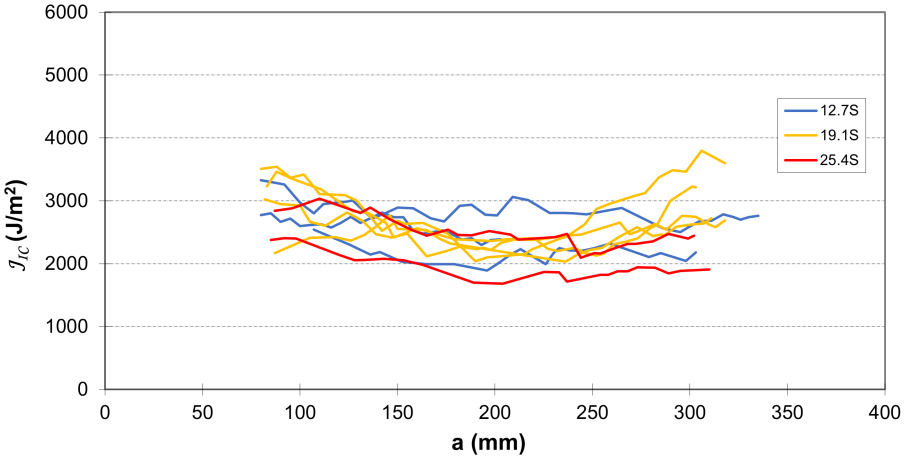

Figure A.17: Paris and Paris J-Integral calculated fracture energy vs measured crack length plot for most DCB specimens.

Society of London. A. Mathematical and Physical Sciences 427 (1990) 173–199.

[2] M. Conroy, A. Kinloch, J. Williams, A. Ivankovic, Mixed mode partitioning of beam-like geometries: A damage dependent solution, Engineering Fracture Mechanics 149 (2015) 351–367.

[3] B. Blackman, H. Hadavinia, A. J. Kinloch, J. Williams, The use of a cohesive zone model to study the fracture of fibre composites and adhesively-bonded joints, International journal of fracture 119 (1) (2003) 25–46.

[4] R. B. Barros, R. D. Campilho, I. J. Sánchez-Arce, J. M. Dionísio, K. Madani, Evaluation of the cracked lap shear test for mixed-mode fracture toughness estimation of adhesive joints, Proceedings of the Institution of Mechanical Engineers, Part L: Journal of Materials: Design and Applications (2022) 14644207221140296.

[5] D. A. Dillard, H. K. Singh, D. J. Pohlit, J. M. Starbuck, Observations of decreased fracture toughness for mixed mode fracture testing of adhesively bonded joints, Journal of Adhesion Science and Technology 23 (2009) 1515–1530.

[6] M. Thouless, Fracture resistance of an adhesive interface, Scripta metallurgica et materialia 26 (6) (1992) 949–951.

[7] M. Conroy, B. Sørensen, A. Ivankovic, Combined numerical and experimental investigation of mode-mixity in beam like geometries, in: Proceedings of the 37th Annual Meeting of the Adhesion Society, Feburary, 2014.

[8] S. Mostovoy, P. Crosley, E. J. Ripling, Use of Crack-Line Loaded Specimen for Measuring Plane-Strain Fracture Toughness, Journal of Materials 2 (1967) 661–681.

[9] M. Kanninen, An augmented double cantilever beam model for studying crack propagation and arrest, International Journal of fracture 9 (1973) 83–92.

[10] L. A. Carlsson, J. Gillespie Jr, R. Pipes, On the analysis and design of the end notched flexure (enf) specimen for mode ii testing, Journal of composite materials 20 (1986) 594–604.

[11] H. Wang, T. Vu-Khanh, Use of end-loaded-split (els) test to study stable fracture behaviour of composites under mode ii loading, Composite Structures 36 (1996) 71–79.

[12] M. Benzeggagh, M. Kenane, Measurement of mixed-mode delamination fracture toughness of unidirectional glass/epoxy composites with mixed-mode bending apparatus, Composites Science and Technology 56 (4) (1996) 439–449.

[13] F. Ducept, D. Gamby, P. Davies, A mixed-mode failure criterion derived from tests on symmetric and asymmetric specimens, Composites science and technology 59 (1999) 609–619.

[14] B. Davidson, V. Sundararaman, A single leg bending test for interfacial fracture toughness determination, International Journal of Fracture 78 (1996) 193–210.

[15] T. R. Brussat, S. T. Chiu, S. Mostovoy, Fracture mechanics for structural adhesive bonds, Report AFNL-TR-77-163, Air Force Materials Laboratory, USA (1977).

[16] Y.-H. Lai, M. D. Rakestraw, D. A. Dillard, The cracked lap shear specimen revisited—a closed form solution, International Journal of Solids and Structures 33 (12) (1996) 1725–1743.

[17] C. Creton, E. J. Kramer, H. R. Brown, C.-Y. Hui, Adhesion and fracture of interfaces between immiscible polymers: from the molecular to the continuum scal, Molecular Simulation Fracture Gel Theory (2001) 53–136.

[18] F. Ducept, D. Gamby, P. Davies, A mixed-mode failure criterion derived from tests on symmetric and asymmetric specimens, Composites science and technology 59 (4) (1999) 609–619.

[19] W. D. Hartley, J. McCann, S. Davis, T. Hocker, S. Bobba, N. Verghese, D. Bajaj, H. Z. Yu, D. A. Dillard, Fracture characterization of overmold composite adhesion, Journal of Thermoplastic Composite Materials (2020) 1–21.

[20] S. Park, D. A. Dillard, Development of a simple mixed-mode fracture test and the resulting fracture energy envelope for an adhesive bond, International Journal of Fracture 148 (2007) 261–271.

[21] R. Moreira, M. de Moura, F. Silva, A novel strategy to obtain the fracture envelope under mixed-mode i+ii loading of composite bonded joints, Engineering Fracture Mechanics 232 (2020) 107032.

[22] G. Fernlund, J. Spelt, Mixed-mode fracture characterization of adhesive joints, Composites science and technology 50 (4) (1994) 441–449.

[23] J. R. Reeder, J. H. Crews Jr, Mixed-mode bending method for delamination testing, AiAA Journal 28 (7) (1990) 1270–1276.

[24] H. K. Singh, A. Chakraborty, C. E. Frazier, D. A. Dillard, Mixed mode fracture testing of adhesively bonded wood specimens using a dual actuator load frame, Holzforschung 64 (3) (2010) 353–361.

[25] B. F. Sørensen, K. Jørgensen, T. K. Jacobsen, R. C. Østergaard, Dcb-specimen loaded with uneven bending moments, International Journal of Fracture 141 (2006) 163–176.

[26] K. M. Liechti, Y.-S. Chai, Biaxial Loading Experiments for Determining Interfacial Fracture Toughness, Journal of Applied Mechanics 58 (1991) 680–687.

[27] J. G. Williams, On the calculation of energy release rates for cracked laminates, International Journal of Fracture 36 (1988) 101–119.

[28] B. Blackman, A. Kinloch, F. Rodriguez-Sanchez, W. Teo, The fracture behaviour of adhesively-bonded composite joints: Effects of rate of test and mode of loading, International Journal of Solids and Structures 49 (2012) 1434–1452.

[29] J. P. Berry, Determination of fracture surface energies by the cleavage technique, Journal of Applied Physics 34 (1963) 62–68.

[30] M. de Moura, M. Silva, A. de Morais, J. Morais, Equivalent crack based mode ii fracture characterization of wood, Engineering Fracture Mechanics 73 (2006) 978–993.

[31] M. de Moura, R. Campilho, J. Gonçalves, Crack equivalent concept applied to the fracture characterization of bonded joints under pure mode i loading, Composites Science and Technology 68 (2008) 2224–2230.

[32] J. M. Oliveira, M. F. de Moura, J. J. Morais, Application of the end loaded split and single-leg bending tests to the mixed-mode fracture characterization of wood, Holzforschung 63 (2009) 597–602.

[33] Imperial College lefm test protocols, https://www.imperial.ac.uk/mechanical-engineering/research/mechanics-of-materials/composites-adhesives-and-soft-solids/adhesion/test-protocols/, accessed: 2022-12-08.

[34] J. R. Rice, A Path Independent Integral and the Approximate Analysis of Strain Concentration by Notches and Cracks, Journal of Applied Mechanics 35 (1968) 379–386.

[35] S. Marzi, Innovations in fracture testing of structural adhesive bonds, in: D. A. Dillard (Ed.), Advances in Structural Adhesive Bonding, 2nd Edition, Elsevier, 2023, pp. ??–??

[36] A. J. Paris, P. C. Paris, Instantaneous evaluation of J and C, International Journal of Fracture 38 (1988) R19–R21.

[37] Y. Zhu, K. M. Liechti, K. Ravi-Chandar, Direct extraction of rate-dependent traction–separation laws for polyurea/steel interfaces, International Journal of Solids and Structures 46 (2009) 31–51.

[38] S. Marzi, A. Biel, U. Stigh, On experimental methods to investigate the effect of layer thickness on the fracture behavior of adhesively bonded joints, International Journal of Adhesion and Adhesives 31 (8) (2011) 840–850.

[39] J. Gorman, M. Thouless, The use of digital-image correlation to investigate the cohesive zone in a double-cantilever beam, with comparisons to numerical and analytical models, Journal of the Mechanics and Physics of Solids 123 (2019) 315–331.

[40] J. Manterola, J. Renart, J. Zurbitu, A. Turon, I. Urresti, Mode i fracture characterisation of rigid and flexible bonded joints using an advanced wedge-driven test, Mechanics of Materials 148 (2020) 103534.

[41] F. Sun, B. R. Blackman, Using digital image correlation to automate the measurement of crack length and fracture energy in the mode i testing of structural adhesive joints, Engineering Fracture Mechanics 255 (2021) 107957.

[42] F. Sun, B. Blackman, A dic method to determine the mode i energy release rate g, the j-integral and the traction-separation law simultaneously for adhesive joints, Engineering Fracture Mechanics 234 (2020) 107097.

[43] M. Bain, Erich Dand Pollum, D. Fortman, M. Losada, C. M. Jackson, R. Jensen, Emerging structural adhesive chemistries and innovations, in: D. A. Dillard (Ed.), Advances in Structural Adhesive Bonding, 2nd Edition, Elsevier, 2023, pp. 221–249.

[44] CCDC ARL, Mil-prf-32662: Adhesive, high-loading rate, for structural and armor applications, Tech. rep., Aberdeen Proving Ground (MD): CCDC Army Research Laboratory (US), Aberdeen, Maryland (2020). URL https://quicksearch.dla.mil/qsDocDetails.aspx?ident_number=283919

[45] Y.-H. Lai, D. A. Dillard, Using the fracture efficiency to compare adhesion tests, International journal of solids and structures 34 (4) (1997) 509–525.

[46] D. Dugdale, Yielding of steel sheets containing slits, Journal of the Mechanics and Physics of Solids 8 (1960) 100–104.

[47] G. Barenblatt, The mathematical theory of equilibrium cracks in brittle fracture, Vol. 7 of Advances in Applied Mechanics, Elsevier, 1962, pp. 55–129.

[48] A. Hillerborg, M. Modéer, P.-E. Petersson, Analysis of crack formation and crack growth in concrete by means of fracture mechanics and finite elements, Cement and Concrete Research 6 (1976) 773–781.

[49] L. F. Da Silva, R. D. Campilho, Advances in numerical modelling of adhesive joints, SpringerBriefs in Computational Mechanics, 2012.

[50] M. Kafkalidis, M. Thouless, The effects of geometry and material properties on the fracture of single lap-shear joints, International Journal of Solids and Structures 39 (17) (2002) 4367–4383.

[51] S. Sugiman, A. Crocombe, I. Aschroft, Modelling the static response of unaged adhesively bonded structures, Engineering Fracture Mechanics 98 (2013) 296–314.

[52] B. Shen, G. Paulino, Direct extraction of cohesive fracture properties from digital image correlation: a hybrid inverse technique, Experimental Mechanics 51 (2011) 143–163.

[53] R. D. Campilho, M. D. Banea, J. Neto, L. F. da Silva, Modelling adhesive joints with cohesive zone models: effect of the cohesive law shape of the adhesive layer, International Journal of Adhesion and Adhesives 44 (2013) 48–56.

[54] S. Rajan, M. A. Sutton, R. Fuerte, A. Kidane, Traction-separation relationship for polymer-modified bitumen under mode i loading: Double cantilever beam experiment with stereo digital image correlation, Engineering Fracture Mechanics 187 (2018) 404–421.

[55] S. Ravindran, S. Sockalingam, K. Kodagali, A. Kidane, M. A. Sutton, B. Justusson, J. Pang, Mode-i behavior of adhesively bonded composite joints at high loading rates, Composites Science and Technology 198 (2020) 108310.

[56] F. Sun, R. Zhang, B. R. Blackman, Determination of the mode i crack tip opening rate and the rate dependent cohesive properties for structural adhesive joints using digital image correlation, International Journal of Solids and Structures 217-218 (2021) 60–73.

[57] J. Xavier, M. Oliveira, J. Morais, M. de Moura, Determining mode ii cohesive law of pinus pinaster by combining the end-notched flexure test with digital image correlation, Construction and Building Materials 71 (2014) 109–115.

[58] F. A. Leone Jr, D. Girolamo, C. G. Davila, Progressive damage analysis of bonded composite joints, Tech. rep., NASA, Langley Research Center Hampton, Virginia 23681-2199 (7 2012).

[59] C. Wu, S. Gowrishankar, R. Huang, K. M. Liechti, On determining mixed-mode traction–separation relations for interfaces, International Journal of Fracture (2016) 1–19.

[60] C. Wu, R. Huang, K. M. Liechti, Simultaneous extraction of tensile and shear interactions at interfaces, Journal of the Mechanics and Physics of Solids 125 (2019) 225–254.

[61] Q. Yang, M. Thouless, S. Ward, Elastic–plastic mode-ii fracture of adhesive joints, International journal of solids and structures 38 (2001) 3251–3262.

[62] S. Azari, A. Ameli, M. Papini, J. Spelt, Analysis and design of adhesively bonded joints for fatigue and fracture loading: a fracture-mechanics approach, Journal of adhesion science and technology 27 (15) (2013) 1681–1711.

[63] Standard Test Method for Apparent Shear Strength of Single-Lap-Joint Adhesively Bonded Metal Specimens by Tension Loading (Metal-to-Metal), Standard, ASTM International, West Consohocken, PA (2010).

[64] R. H. Plaut, D. Hwang, C. Lee, M. D. Bartlett, D. A. Dillard, Peeling of finite-length elastica on winkler foundation until complete detachment, International Journal of Solids and Structures 256 (2022) 111944.

[65] B. Blackman, A. Kinloch, M. Paraschi, W. Teo, Measuring the mode i adhesive fracture energy, gic, of structural adhesive joints: the results of an international round-robin, International Journal of Adhesion and Adhesives 23 (2003) 293–305.

[66] M. May, H. Voß, S. Hiermaier, Predictive modeling of damage and failure in adhesively bonded metallic joints using cohesive interface elements, International Journal of Adhesion and Adhesives 49 (2014) 7–17.

[67] H. Khoramishad, Modelling fatigue damage in adhesively bonded joints, Ph.D. thesis, University of Surrey (United Kingdom) (2010).

[68] M. De Moura, J. Gonçalves, F. Silva, A new energy based mixed-mode cohesive zone model, International Journal of Solids and Structures 102 (2016) 112–119.

[69] N. Moës, T. Belytschko, Extended finite element method for cohesive crack growth, Engineering Fracture Mechanics 69 (7) (2002) 813–833.

[70] A. Turon, C. Dávila, P. Camanho, J. Costa, An engineering solution for mesh size effects in the simulation of delamination using cohesive zone models, Engineering Fracture Mechanics 74 (2007) 1665–1682.

[71] H. Chai, Shear fracture, International Journal of Fracture 37 (1988) 137–159.

[72] H. A. M. Araújo, Impact and damping behaviour of composite adhesive joints (2016).

[73] I. Q. Vu, L. B. Bass, C. B. Williams, D. A. Dillard, Characterizing the effect of print orientation on interface integrity of multi-material jetting additive manufacturing, Additive Manufacturing 22 (2018) 447–461.

[74] S. Li, J. Wang, M. Thouless, The effects of shear on delamination in layered materials, Journal of the Mechanics and Physics of Solids 52 (1) (2004) 193–214.

[75] A. D3433-99, Standard test method for fracture strength in cleavage of adhesives in bonded metal joints, Adhesives, American Society for Testing and Materials (1999).

[76] M. Thouless, Shear forces, root rotations, phase angles and delamination of layered materials, Engineering Fracture Mechanics 191 (2018) 153–167.

[77] G. Alfano, On the influence of the shape of the interface law on the application of cohesive-zone models, Composites Science and Technology 66 (2006) 723–730.

[78] P. Bamberg, U. Reisgen, A. Schiebahn, J. Barbosa, B. Marx, R. Coelho, Digital image correlation analysis of the effects of the overlap length, adhesive thickness and adherends yield strength over similar and dissimilar joints of high strength steel and aluminum alloys, International Journal of adhesion and adhesives 83 (2018) 69–75.

[79] E. Winkler, Die Lehre von der Elasticitaet und Festigkeit: mit besonderer Rücksicht auf ihre Anwendung in der Technik, für polytechnische Schulen, Bauakademien, Ingenieure, Maschinenbauer, Architecten, etc, H. Dominicus, 1867.

[80] D. A. Dillard, B. Mukherjee, P. Karnal, R. Batra, J. Frechette, A review of winkler's foundation and its profound influence on adhesion and soft matter applications, Soft Matter 14 (2018) 3669–3683.

[81] M. D. Banea, L. F. M. da Silva, R. Carbas, R. D. S. G. Campilho, Effect of material on the mechanical behaviour of adhesive joints for the automotive industry, Journal of Adhesion Science and Technology 31 (6) (2017) 663–676.

[82] L. J. Hart-Smith, Adhesive-bonded single-lap joints, Tech. rep. (1973).

[83] C. M. Jackson, Experimental and numerical methods for characterizing the mixed-mode fracture envelope for a tough epoxy, Ph.D. thesis, Virginia Tech (2022).